Available online at www.sciencedirect.com
SCIENCE DIRECT®
International Journal of Heat and Mass Transfer 49 (2006) 3142–3155
International Journal of HEAT and MASS TRANSFER
www.elsevier.com/locate/ijhmt

Convective flow of refrigerant (R-123) across a bank of micro pin fins

Ali Koşar, Yoav Peles *

Department of Mechanical, Aerospace and Nuclear Engineering, Rensselaer Polytechnic Institute, Troy, NY 12180, USA

Received 18 April 2005; received in revised form 22 December 2005
Available online 5 April 2006

Abstract

An experimental study has been performed on single-phase heat transfer, boiling inception, and pressure drop of R-123 over a bank of shrouded micro pin fins 243 μm long with hydraulic diameter of 99.5 μm. Heat transfer coefficients and Nusselt numbers have been obtained over effective heat fluxes ranging from 3.5 to 65.5 W/cm^2 and Reynolds numbers from 134 to 314. A delay in boiling incipience has been observed and a meta-stable single-phase region was apparent at liquid exit temperatures noticeably exceeding the saturation temperature. Once boiling was initiated, vapor burst instabilities resembling the *compound relaxation instabilities* were attained. It has also been found that endwalls effects on heat transfer diminished for $Re > 100$.

Keywords: MEMS; Heat sink; Pin fin; Cross flow; Boiling; Single-phase; Flow instabilities

1. Introduction

Heat transfer in MicroElectroMechanical Systems (MEMS) has been a topic of extensive studies over the last decade. Numerous investigations have been devoted to unveil the thermal performance of abundant micro systems for the use of various applications stretched across assorted technological disciplines, such as micro rockets [1,2], micro combustors [3,4], electronic chip cooling systems [5–10], micro chemical reactors [11,12], micro heat engines [13], etc. With the maturity of the field, more sophisticated second-generation enhanced heat transfer systems are emerging. Flow over silicon micro pin fins has surfaced as a facilitating method in diverse applications [1,5,12,14] to augment systems' thermal-hydraulic and chemical performance. To better engineer and gain physical insight into the performance of these systems, researchers and designers resort to correlations already available in the literature for large scale systems. While this approach is justifiable for first-generation systems, more accurate correlations and models need to be developed and used in the subsequent generation, especially because considerable anomalies have been reported between conventional and micro scale fluid flow and heat transfer in MEMS devices.

Heat transfer and pressure drop over a bank of long tube bundles have been a subject of intense investigations over the last century and many correlations and models [15] were developed to ameliorate the design of numerous heat exchangers. Flow over intermediate size pin fin ($1/2 <$ height-to-diameter < 6) heat sinks have been mainly studied in the context of turbine blade cooling. Nusselt number and friction factor correlations for circular [16,17], rectangular [18,19], and diamond [20] intermediate size pin fins have been developed. Other aspects of the thermal-hydraulic performance of intermediate size pin fins were also examined such as tip clearance [21]. Driven by a specific application, the vast majority of studies on pin fins having height-to-diameter ratios smaller than 6 were concerned with the thermal performance of air flow at turbulent flow conditions (Reynolds number larger than ~1000). Thus, the existing data and knowledge available in the literature can be exploited to extract qualitative insight into the heat transfer and fluid flow characteristics of flow over micro scale pin fin heat sinks, but much less for quantitative evaluation.

* Corresponding author. Tel.: +1 518 276 2886; fax: +1 518 276 2623.
E-mail address: pelesy@rpi.edu (Y. Peles).

0017-9310/$ - see front matter © 2006 Elsevier Ltd. All rights reserved.
doi:10.1016/j.ijheatmasstransfer.2006.02.013

Nomenclature

A_p	planform area, m^2
A_t	total heat transfer area, m^2
C	constant
c_p	specific heat at constant pressure, kJ kg^{-1} °C^{-1}
d	pin fin diameter, m
G	mass velocity, kg m^{-2} s^{-1}
$\bar{h}$	average heat transfer coefficient, W m^{-2} °C^{-1}
H	channel height, fin height, m
h_{FG}	latent heat of evaporation, kJ kg^{-1}
I	current, A
k_{fin}	thermal conductivity of the fin (silicon), W m °C^{-1}
k_{fluid}	thermal conductivity of the fluid, W m °C^{-1}
k_s	thermal conductivity of the surface, W m °C^{-1}
L	channel length, m
m	constant
$\dot{m}$	mass flow rate, kg s^{-1}
m_f	fin parameter in Eq. (4)
M	number of data points at a fixed flow rate (Eq. (6)), total number of data points (Eq. (7))
M_W	molar weight, kg/kmol
MAE	mean absolute error
n	constant
N_t	total number of pin fins
Nu_{av}	Nusselt number evaluated at average temperature
$\overline{Nu}$	average Nusselt number
p	pressure, kPa
p_{cr}	critical pressure, kPa
P	electrical power, W
Pr	Prandtl number
q''	effective heat flux, W cm^{-2}
q''_{ch}	heat flux based on A_t, W cm^{-2}
$\dot{Q}$	volumetric flow rate, m^3 s^{-1}
$\dot{Q}_{loss}$	heat loss, W
r	cavity radius, m
r_{cr}	critical radius, m
r_f	characteristic surface cavity radius, m
R	electrical resistance, Ω
$\overline{R}$	ideal gas constant, kJ $kmol^{-1}$ K^{-1}
Re	Reynolds number based on the pin fin diameter
S_L	longitudinal pitch, m
S_T	transverse pitch, m
t	thickness of the silicon block, m
T	temperature, °C
$\overline{T}$	average surface temperature, °C
T_e	exit fluid temperature, °C
T_i	inlet fluid temperature, °C
$T_{s,e}$	exit surface temperature, °C
T_{SAT}	saturation temperature, °C
U	parameter being evaluated
V	voltage, Volts
w	channel width, m

Greek symbols

Δp	pressure drop, kPa
$\Delta T_{SAT,e}$	temperature difference between $T_{s,e}$ and T_{SAT}, °C
ξ_{cr}	parameter in Eq. (11)
η_f	fin efficiency
μ	viscosity, kg m^{-1} s^{-1}
ρ	density, kg m^{-3}
ρ_{cr}	critical density, kg m^{-3}
σ	surface tension, N m^{-1}

Subscripts

amb	ambient
av	average
c	cavity
cr	critical
e	exit
exp	experimental
f	fluid
fin	fin
i	inlet
j	index in Eq. (6)
L	liquid
ONB	onset of nucleate boiling
pred	predicted
s	surface
SAT	saturation

Thermal-hydraulic performance of miniature scale pin fin heat sinks has recently been examined by several investigators. Marques and Kelly [22] extended the knowledge of convective heat transfer over pin fins to the mini/micro scale, while Peles et al. [5] examined similar systems at the micro scale (50–100 μm hydraulic diameter pin fins). They provided supporting evidence that single-phase flow over micro scale pin fin heat sinks results in superior thermal and hydraulic performance compared to microchannel flow. In a subsequent paper, Koşar and Peles [23] tested water flow at Reynolds numbers up to 112 over pin fins having a height-to-diameter ratio of 2.43, and found that for Reynolds numbers below ~50 conventional scale long tube correlations considerably overpredicted heat transfer coefficients, while for larger Reynolds numbers the prediction was considerably better. Endwalls effects were designated as the primary cause for this anomaly. It was argued that the Prandtl number will affect the heat transfer coefficient in a manner not fully envisioned. Friction factors were also obtained [24,25] for micro scale pin fin heat sinks, and similar to the heat transfer coefficient, deviations from long tube data at low fin height-to-diameter ratios

were registered at low Reynolds numbers. Koşar [26] presented a performance evaluation study over five assorted MEMS-based pin fin heat sinks of different spacing, arrangements and shapes. It was found that the effects of spacing, shape of pin fins, and arrangement on friction factor and heat transfer were in agreement with existing large scale literature.

It is argued that micro scale pin fin heat sinks hold great potential as an enabling technology for numerous high heat dissipation power systems. However, little is known about the thermal performance of such neoteric devices at a diminishing length scale. Thus, the present study aims at obtaining the heat transfer characteristics of R-123 coolant over a miniature size pin fin heat sink at moderate laminar Reynolds numbers. Two-phase flow instabilities, as well as boiling inception, have been discussed and compared to conventional as well as micro scale results. Heat transfer coefficients, onset of nucleate boiling, and pressure drops have been elucidated as a function of various flow rates and heat fluxes.

2. Fabrication and overview of the micro pin fin device

In the fabrication process, a double side polished, n-type $\langle 1\,0\,0\rangle$ single crystal silicon wafer is processed on both sides to create a MEMS device, which consists of a microchannel enclosing an array of fins. First, the top side and bottom side masks are processed. A 1 μm thick thermal oxide is deposited on both sides of the silicon wafer to protect the bare wafer surface. The heater and the vias are formed on the backside of the wafer by cryopumped CVC 601 sputter deposition system. A 70 Å thick layer of titanium is initially deposited to enhance adhesion characteristics. This process is followed by sputtering a 1 μm thick layer of aluminum containing 1% silicon and 4% copper. Subsequent photolithography and concomitant wet bench processing create the heater on the backside of the wafer. Next, the microchannel with micro pin fins is formed on the top side of the wafer. In order to achieve this, the wafer is taken through a photolithography step and a reactive ion etching (RIE) oxide removal process to mask certain areas on the wafer, which are not to be etched during the deep reactive ion etching (DRIE) process. The wafer is then etched in a DRIE process, and silicon is removed from places not protected by the photoresist/oxide mask. The DRIE process forms deep vertical trenches on the silicon wafer with a characteristic scalloped sidewall possessing a peak-to-peak roughness of ~0.3 μm. A profilometer and an SEM are utilized to measure and record various dimensions of the device. Thereafter, the wafer is flipped and the backside is then processed, so that an inlet, exit, side air gap, and pressure port taps for the transducers are fabricated. A photolithography followed by a buffered oxide etch (BOE) (6:1) oxide removal process is carried out to create a pattern mask. The wafer is then etched-through in a DRIE process to create the fluidic ports. Thereafter, electrical contacts/pads are opened on the backside of the wafer by performing another round of photolithography and RIE processing. Finally, the processed wafer is stripped of any remaining resist or oxide layers and anodically bonded to a 1 mm thick polished Pyrex (glass) wafer to form a sealed device. After successful completion of the bonding process, the processed stack is die-sawed to separate each device from the parent wafer.

A computer aided design (CAD) image of the resulting device consisting of a 1800 μm wide and a 1 cm long microchannel of depth 243 μm is shown in Fig. 1. The microchannel contains an array of 12 and 13 (in tandem) 99.5 μm diameter circular pin fins with equal longitudinal and transverse spacing ($S_T = S_L$) of 150 μm. In order to minimize ambient heat losses an air gap is formed on the two ends of the side walls, and an inlet and exit plenum, 4 mm long each, are etched on the thin silicon substrate (~150 μm). A heater acting as a thermistor for temperature measurements is deposited on the backside to deliver the heating power. A Pyrex cover seals the device from the top and allows flow visualization. Pressure taps are created at the inlet and exit of the device.

3. Experimental setup and procedure

In Fig. 2, a schematic of the experimental setup is shown. Major components are the pump, filter, flowmeter (rotameter), packaging module, and micro pin fin device. The micro pin fin device is packaged by sandwiching it between two plates, as shown in Fig. 3. The fluidic seals are forged using miniature "o-rings". The external electrical connections to the heater are installed from beneath through spring-loaded pins, which connect the heater to electrical pads residing away from the main micro pin fin device body. Resistance, pressure, and flow measurements are taken at a fixed flow rate in the loop. The electrical power is supplied to the device with an INSTEK programmable power supply, while electrical current and voltage are measured through an accurate HP digital multimeter. A HNP Mikrosysteme micro annular gear pump capable of generating flowrates from 0.3 to 18 ml/min is used to propel the liquid from a reservoir through the MEMS device at various flow rates. Inlet and exit pressures are measured via pressure transducers. An Omega F-111 flow meter is calibrated with respect to the working fluid (R-123), and the resulting calibration curve is used to convert the flow meter reading to the volumetric flow rate. Pressure and flow rate data are acquired together with the voltage and current data to the spreadsheet file for data reduction. The flow is proctored with a microscope and flow images are taken via a Vision Research Phantom V-4 series high-speed camera capable of capturing frames with a rate up to 90,000 frames/s, a maximum resolution of 512×512 pixels, and a minimum exposure time of 2 μs.

In the experimental procedure, the flow rate is first fixed at the desired value, and data are taken after steady flow conditions are reached under exit pressure of 267 kPa.

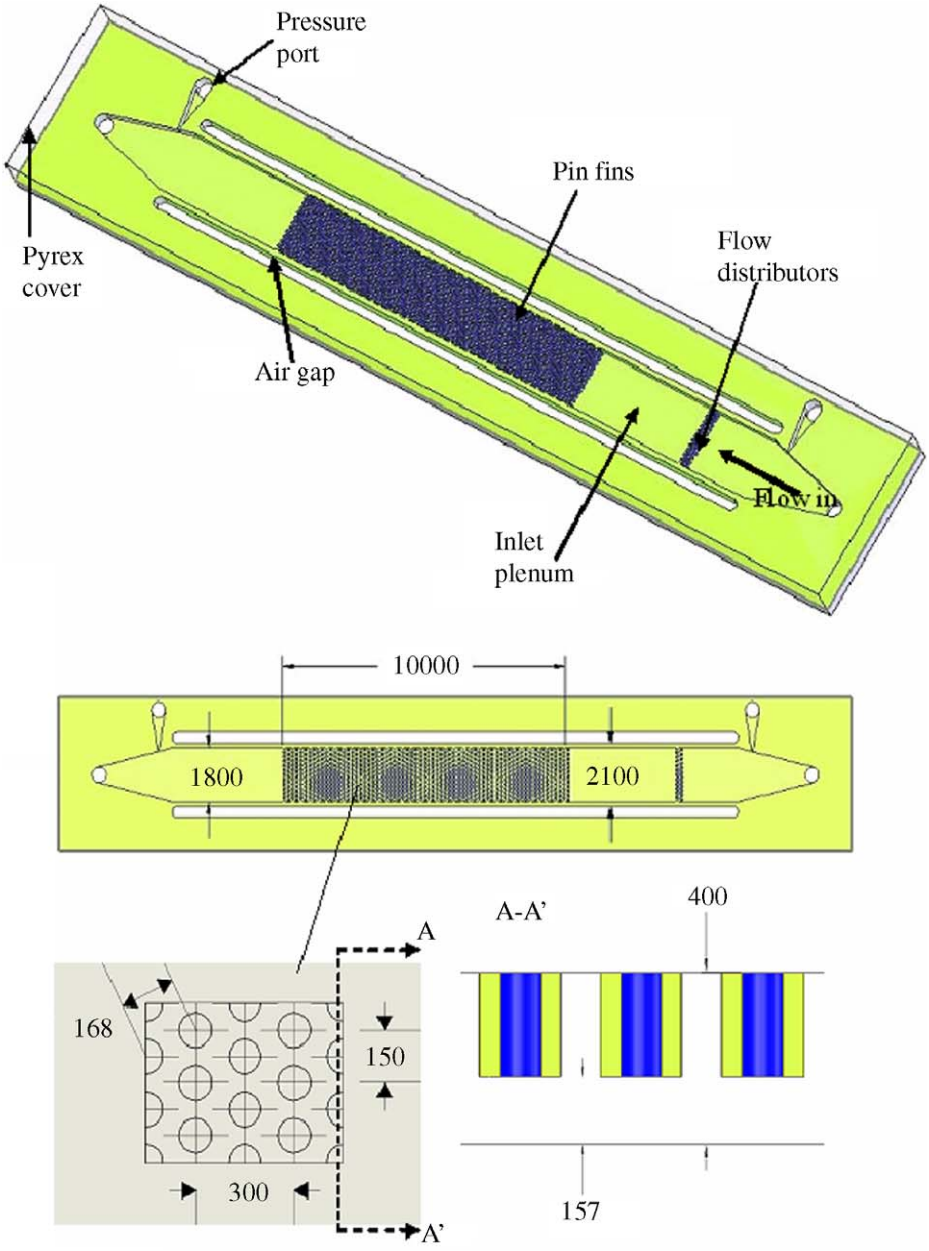

Fig. 1. (a) CAD model of the micro pin fin heat sink. (b) Top view of the device (dimensions in μm).

R-123 is utilized as the working fluid. Before taking any data the device was calibrated in a well insulated and temperature controlled oven, and the heater electrical resistance–temperature linear calibration curve (Fig. 4) was generated. A standard deviation of 0.16 °C was obtained between the individual data points and the calibration curve. The resulting calibration curve is then used during data reduction to find the average temperature of the device.

Prior to acquiring experimental data the electrical resistance of the heater was measured at room temperature. The flow meter reading is adjusted to the desired flow rate, and the pressure difference between the inlet and exit pressure ports is recorded through a LabView® interface to a spreadsheet file. This procedure is followed until all the pressure differences corresponding to desired flow rates are recorded. To obtain heat transfer data, voltage is applied in 0.5 V increments across the heater, and the current/voltage data are recorded while ensuring the constancy of the flow rate. The voltage was monotonically increased, until a surge in the resistance corresponding to an abrupt temperature rise was detected. At this condition, the power is switched off to secure the device. The same procedure is repeated for all other flow rates.

4. Data reduction and uncertainty analysis

The data obtained from the voltage, current, and flow rate measurements are reduced to the average wall

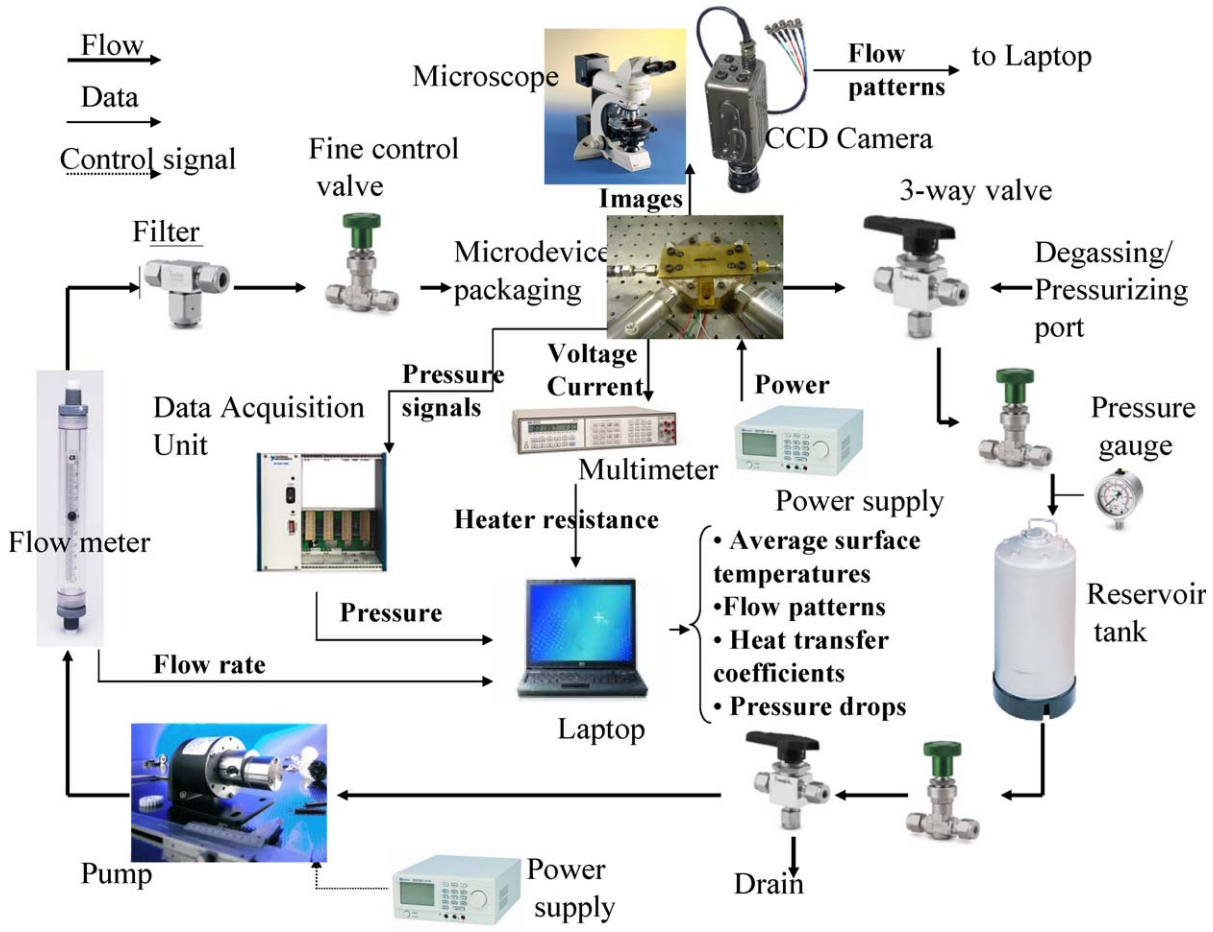

Fig. 2. Experimental setup.

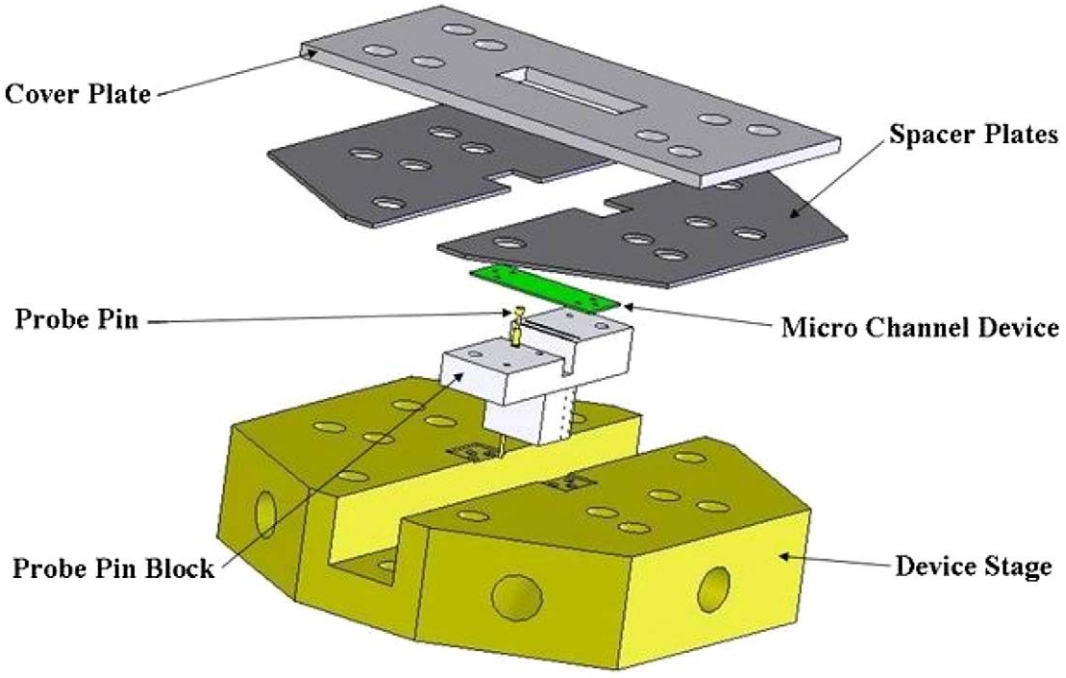

Fig. 3. Device package.

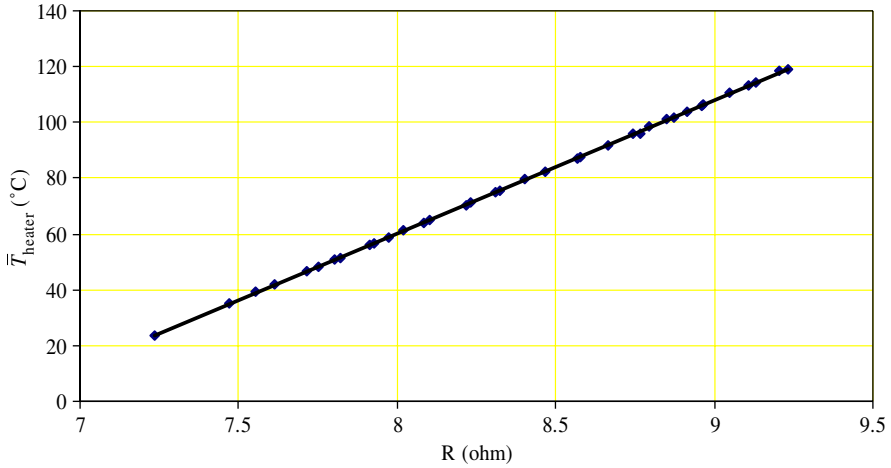

Fig. 4. Electrical resistance–temperature linear calibration curve.

temperatures and heat transfer coefficients. The electrical input power and resistance can be found as, respectively:

$$P = V \times I \tag{1}$$

and

$$R = V/I \tag{2}$$

Average heater temperature is found using electrical resistance. Under the 1-D steady state heat conduction assumption, the surface temperature at the base of the microchannels is expressed as

$$\overline{T} = \overline{T}_{\text{heater}} - \frac{(P - \dot{Q}_{\text{loss}})t}{k_s A_p} \tag{3}$$

The Biot number for the thin silicon substrate region was estimated and was found to be between 20 and 40. Thus, it may be concluded that constant heat flux is a fairly reasonably assumption. The heat transfer analysis presented below is based on the constant heat flux boundary condition.

4.1. Heat transfer

The heat transfer coefficient is found using Newton's law of cooling jointly with 1-D steady-state adiabatic tip fin equation as follows:

$$(P - \dot{Q}_{\text{loss}}) = \bar{h}\left(\eta_f N_t \pi d H + wL - N_t \frac{\pi d^2}{4}\right)\left[\overline{T} - \left(\frac{T_i + T_e}{2}\right)\right] \tag{4}$$

where $\eta_f = \frac{\tanh(m_f H)}{m_f H}$, $T_e = T_i + \frac{P - \dot{Q}_{\text{loss}}}{\dot{m} c_p}$, and $m_f = 2\sqrt{\frac{\bar{h}}{k_{\text{fin}} d}}$.

Eq. (4) is solved iteratively to obtain $\bar{h}$. Nusselt number corresponding to each net input power at a fixed flow rate can be calculated using the average heat transfer coefficient obtained from Eq. (4) as

$$(Nu)_{\text{av}} = \frac{\bar{h} d}{k_{\text{fluid}}} \tag{5}$$

Table 1
Experimental uncertainties

Uncertainty	Error
Flow rate, Q (for each reading)	±1.0%
Voltage supplied by power source, V	±0.1%
Current supplied by power source, I	±0.1%
Ambient temperature, T_{amb}	±0.1 °C
Electrical power, P	±0.15%
Electrical resistance, R	±0.15%
Average temperature, $\overline{T}$	±0.5 °C
Pressure drop, Δp	±0.25%
Average Nusselt number, $\overline{Nu}$	±13.0%

An average value of the average Nusselt number over all heat fluxes for a fixed Reynolds number is then calculated according to:

$$\overline{Nu} = \frac{1}{M}\sum_{j=1}^{M}(Nu)_{\text{av},j} \tag{6}$$

4.2. Uncertainty analysis

The uncertainties of the measured values, given in Table 1, are obtained from the manufacturer's specification sheets, while the uncertainties of the derived parameters are calculated using the method developed by Kline and McClintock [27]. The comparison of the experimental data with existing correlations is accomplished through the mean absolute error (MAE) defined as

$$\text{MAE} = \frac{1}{M}\sum_{j=1}^{M}\frac{|U_{\text{exp}} - U_{\text{pred}}|}{U_{\text{exp}}} \times 100\% \tag{7}$$

5. Results and discussion

Resistance data have been reduced to obtain average wall temperatures, which are necessary to perform heat transfer analysis. Average wall temperature as a function of heat flux is shown in Fig. 5. A typical linear $\overline{T} - q''$ curve

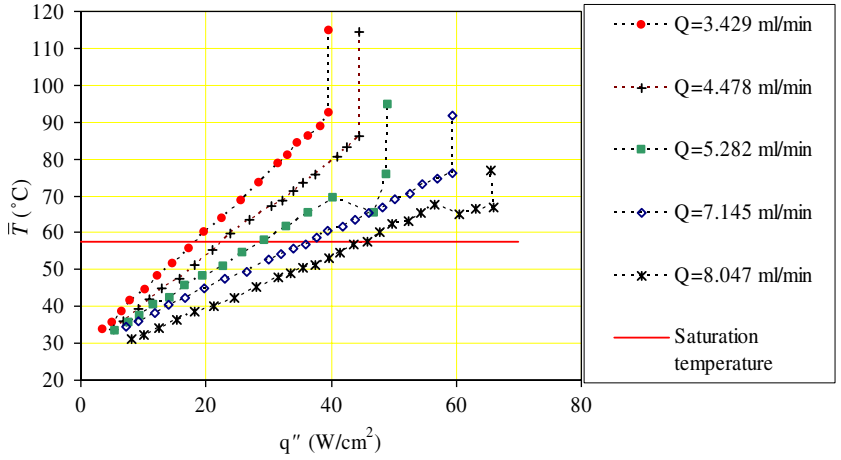

Fig. 5. $\overline{T}$ (°C) vs. q'' profile.

is notable, which is a characteristic of constant heat flux single-phase flow. As expected, a decrease in the slope is obtained as the flow rate increases. The linear increase in the surface temperature continues considerably beyond the corresponding liquid saturation temperature. Flow visualization confirms the dominance of single-phase flow without an apparent phase change. At some critical conditions a meager increase in heat flux triggers an abrupt and intense boiling with considerable increase in the surface temperature and pressure drop marking the arrival of flow instabilities. Boiling conditions are accommodated with significant flow, pressure, and temperature oscillations. These flow characteristics were observed under all flow rates with a minor exception at $Q = 8.047$ ml/min and $Q = 5.282$ ml/min, where a relatively short stable boiling region was detected. However, as heat flux was further increased flow instability conditions were inevitable. With the exception of $Q = 5.282$ ml/min, the maximum surface temperature under single-phase conditions reduced with increasing flow rate. In an attempt to quantify the maximum attained single-phase liquid temperature (maximum meta-stable temperature), the exit liquid and surface temperatures under the conditions of Fig. 5 are shown in Fig. 6. Also shown in the figure is the homogeneous nucleation temperature (161.5 °C), which is given by Waals and Berthelot [28] as

$$\left(\frac{p}{p_{cr}} + \frac{3}{(T_L/T_{cr})^n(\rho_{cr}/\rho)^2}\right)\left(\frac{\rho_{cr}}{\rho} - \frac{1}{3}\right) = \frac{8}{3}\frac{T_L}{T_{cr}} \tag{8}$$

$$\left(\frac{T_L}{T_{cr}}\right)^{1+n} = \frac{[3(\rho_{cr}/\rho) - 1]^2}{4(\rho_{cr}/\rho)^3} \quad \text{where } n = 0.5 \tag{9}$$

As can be seen in Fig. 6b the superheat temperatures required for the onset of nucleate boiling (ONB) are a considerable fraction of the homogeneous nucleation temperature, accentuating the severity of boiling suppression.

As discussed by Bergles [29], with the increase in flow velocities smaller nucleation cavities are activated at the point of boiling inception, which can explain the reduction of boiling inception temperature at higher flow rates. As argued by Bergles and Kandlikar [30] for the low flow velocity encountered in microchannels (the argument can be extended to other micro scale configurations) very large cavities at the point of inception are required. However, since the DRIE etching tool forms characteristic scalloped sidewalls possessing a peak-to-peak roughness of only ~0.3 μm, it follows that ONB is triggered at high superheated temperatures. Perhaps enhanced boiling surfaces such as those proposed by Koşar et al. [31,32] and Zhang et al. [33] might assist to mitigate this temperature overshooting, and thereby delaying flow instabilities.

Regardless of the argument provided above, boiling inception superheat values at the scale observed in the current experiment have not been reported in most of the studies concerning water boiling in microchannels. This excessive superheat at impeding boiling inception is perhaps closely linked to the choice of working liquid. R-123 is a fluorocarbon liquid possessing near-zero contact angle on most engineering surfaces (including native oxide silicon surface). As argued by Bouré et al. [34], for liquids possessing such good wettability characteristics, all of the larger surface cavities may be flooded with the result that a high superheat is required for nucleation. Following this argument, it can be inferred that the vapor/undissolved gas cavities trapped in the surface are considerably smaller than the characteristic surface roughness, and therefore are surrounded by stationary liquid at a near constant temperature equal to the surface temperature as schematically shown in Fig. 7. For highly hydrophilic liquids the contact angle (θ) is near-zero. If the cavity opening angle (β) is small, the critical radius necessary for ONB can be obtained by the expression given in [35]:

$$r_{cr} = \frac{2\overline{R}T_{SAT}^2\sigma}{h_{FG}M_W p\Delta T_{SAT,e}} \tag{10}$$

The corresponding values for the various flow rates at impeding boiling are shown in Fig. 8. The results clearly lend support to the hypothesis linking the excessive superheat at boiling inception with a radical deficit in the nucleation site. All the critical radii are considerably smaller than the characteristic surface cavity ($r_f = 0.3$ μm).

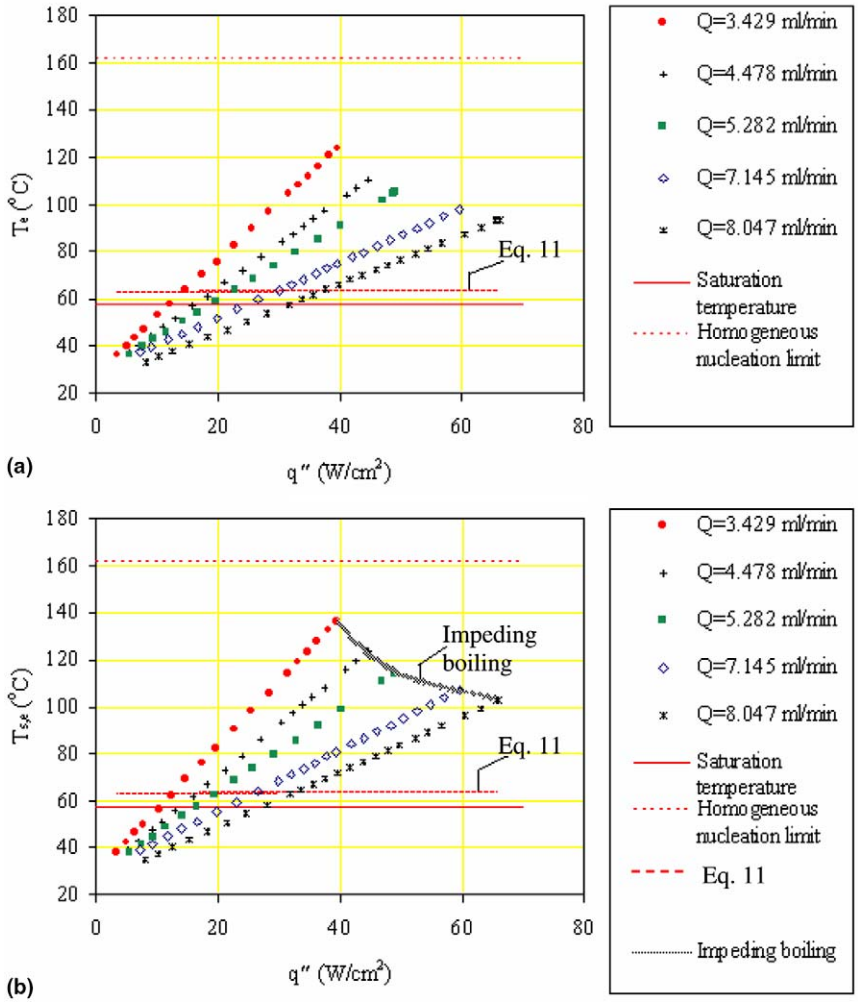

Fig. 6. (a) T_e (°C) vs. q'' profile. (b) T_{se} (°C) vs. q'' profile. T_e (°C) and T_{se} (°C) as a function of q''.

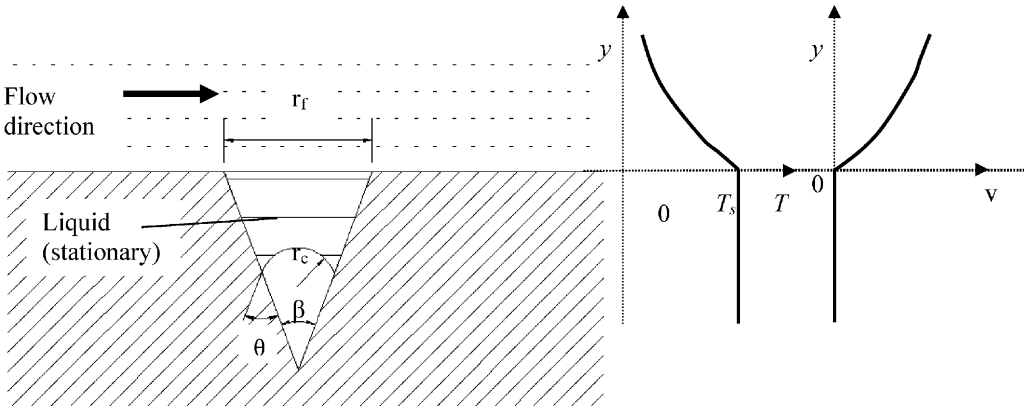

Fig. 7. Vapor cavity trapped inside surface crave.

In the above analysis it was implicitly assumed that the conditions limiting ONB lie within the surface fissure. Namely, the thermal-hydraulic condition in the bulk channel flow (i.e., $y \geqslant 0$ in Fig. 7) is such that once the critical condition is breached inside the surface crater, the bubble will grow undisturbingly beyond the region adjacent to the wall surface. To verify the above assumption Davis and Anderson [36] analytical solution for Hsu and Graham [37] model given in the following form is employed:

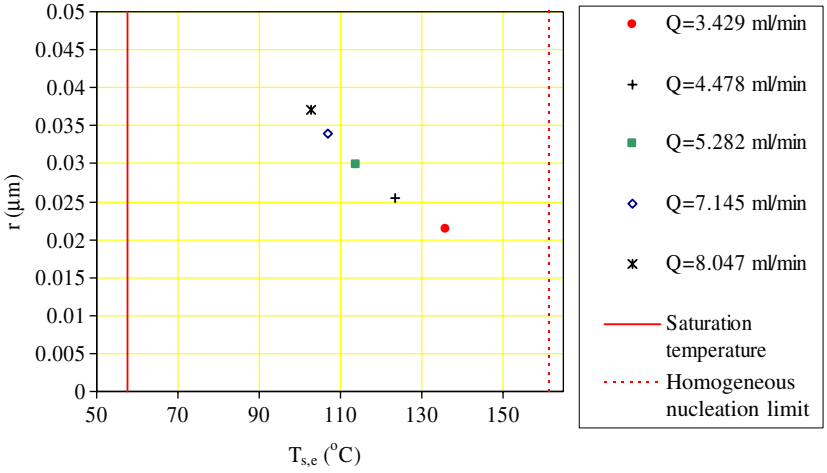

Fig. 8. Critical radius as a function of the exit surface temperature.

$$(\Delta T_{SAT})_{ONB} = \frac{[(\overline{R}T_{SAT}^2)/M_W h_{FG} \ln(1+\xi_{cr})]}{[1-\ln(1+\xi_{cr})(\overline{R}T_{SAT})/M_W h_{FG}]} + \frac{q''_{ch} r_{cr}}{k_{fluid}}$$
$$\text{where } \zeta_{cr} = \frac{2\sigma}{p r_{cr}} \quad (11)$$

Using the characteristic surface roughness (i.e., $r_c = r_f = 0.3$ μm) to estimate the superheat conditions necessary to incept boiling yields considerably lower values ($5.32\ ^\circ\text{C} < (\Delta T_{SAT})_{ONB} < 6\ ^\circ\text{C}$) than the measured temperatures as shown in Fig. 6 (the curve designated as Eq. (11)). Since the pressure drops were considerably smaller than the exit pressure (<25 kPa), the variation of the pressure related properties of the liquid was negligible. Therefore, it was considered to assume a constant value.

With the inception of boiling vapor burst instabilities are initiated, which are characterized by a sudden appearance and rapid growth of the vapor phase in liquid, where high values of superheat wave have been achieved. The explosive-like vapor growth seems to be periodic in nature. A sequence of images over a cycle at boiling inception for mass velocities of 351, 752, and 887 kg/m^2 s is given in Fig. 9. The periods of the vapor growth cycle were measured as 20.08 ms, 13.27 ms, and 12.41 ms, respectively. As can be seen from Fig. 9, initially a vapor cavity is formed at the exit region, which triggers a violent and rapid bubble growth upstream creating a temporary dryout condition downstream. The growth is such that a vapor slug penetrates deep into the inlet plenum. The slug eventually is pushed downstream by the action of the drag force, and liquid replenishes the heat sink completely before a subsequent vapor eruption cycle begins. Unlike many reported microchannel boiling flow oscillations [38–41], no apparent flow reversal was observed and the vigorous vapor growth apparently resulted from rapid vaporization. While attempting to find analogous flow instabilities at conventional scale, the *compound relaxation instability* (specifically *chugging*), which is a part of the larger group of *static instabilities* seems to best resemble the observed flow oscillation trends. The appearance of the vapor cavity triggers other nucleation sites to become active, which might result in the familiar temperature overshoot and boiling curve hysteresis. Since boiling inception was accompanied by flow instabilities, an attempt to obtain the flow hysteresis curve by reducing heat flux jeopardizes the integrity of the device. Indeed, attempting to generate a boiling curve by reversing the heat flux resulted in complete burnout of the heater and the destruction of the test specimen.

The delay in boiling to high superheats triggers a chain of events that perhaps resulted in early critical heat flux (CHF) conditions. Instabilities of large magnitude can lead to early CHF [42]. As noted in several publications [42–44], this is expected to be more prevalent at low flow rates, which might explain the stable (although quite limited) boiling region at high flow rates.

5.1. Single-phase heat transfer

Fig. 10 shows the $\overline{Nu}$ as a function of the Reynolds number along with the Zukauskas [16] correlation obtained on conventional scale apparatus, which is provided in Table 2. This correlation was chosen because it represents the best available prediction tool for the current experimental conditions, since it is applicable for low Reynolds numbers ($10 < Re < 1000$) and all liquids, although it is recommended for long tubes ($H/d > 8$). Also shown in the figure are experimental results obtained in a previous study [23] on a similar device with water at low Reynolds number. Although, Koşar and Peles [23] suggested that due to endwalls effects the Prandtl number might affect the Nusselt number in a manner which deviates from the typical Pr-power law (i.e., Pr^n, $0.3 < n < 0.4$) at low Reynolds numbers, to provide proper comparison to large scale results it is opposite to present the data in the present form. As predicted by Koşar and Peles [23], with the increase of Reynolds number the Nu–Re slope tends to merge to the long tube trend (i.e., the Reynolds power-law lessens) particularly for $Re > 100$ as a result of diminishing endwalls effects. At low Reynolds numbers ($Re < 100$), the correlations considerably underpredict the experimental data.

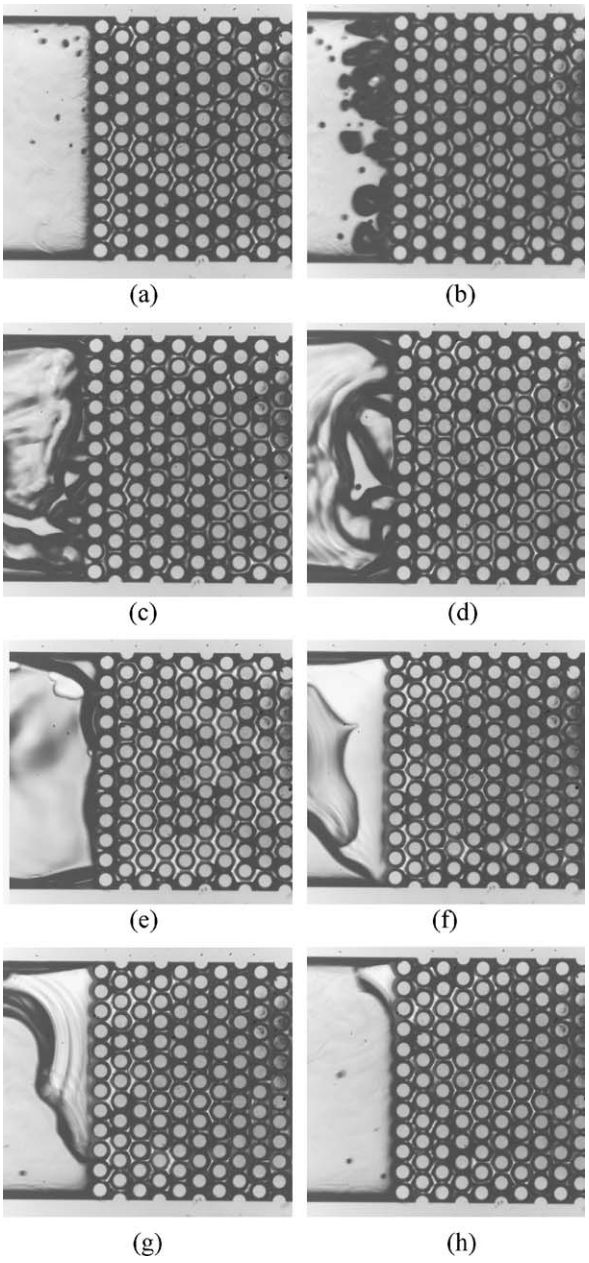

Fig. 9. (a) $t = 0$ ms, (b) $t = 1$ ms, (c) $t = 2.85$ ms, (d) $t = 4.73$ ms, (e) $t = 11.01$ ms, (f) $t = 11.48$ ms, (g) $t = 11.96$ ms, (h) $t = 12.41$ ms. Unstable boiling images recorded for the micro pin fin device (G=887 kg/m^2 s).

The curve obtained for the R-123 experiments naturally follows the Reynolds number trajectory set by the results for water, reconfirming the weakening of endwalls effects at high Reynolds numbers ($Re > 100$). The predictions of the Zukauskas [16] correlation are significantly better for the experimental data of R-123 than for water. The MAE for R-123 data was 15.5%, while the MAE for water was 192.4%.

The liquid properties (e.g., viscosity, Prandtl number, etc.) presented above are based on the inlet conditions. This provides a useful and simple engineering tool to predict the Nusselt number. However, in order to account for the variations in Reynolds and Prandtl numbers (which are mostly secondary) with temperature, the individual data points were evaluated at the mean liquid temperature value (average between inlet and exit temperatures) excluding Pr_s, which was evaluated based on the mean surface temperature. The resulting data were then plotted in Fig. 11a (for R-123) and Fig. 11b (for water) as a function of Zukauskas [16] long tube correlation with a different constant C. Most of the R-123 data fall within the ±20% error band. Significant amount of water data, however, are outside the ±20% error band, particularly at low mass flux (low Reynolds numbers). All the water data at $G < 327$ kg/m^2 s fall outside the ±20% error band, whereas most of the water data at $G > 327$ kg/m^2 s are predicted within ±20%. This trend clearly indicates the predominance of endwalls effects at low Reynolds numbers for water. For R-123, on the other hand, approximately 75% of all data fall within ±20%, implying the diminishing importance of endwalls effects.

Since Zukauskas [16] correlation did not adequately predict the experimental results, especially at low Reynolds numbers, a modification, using the best curve fit approach, was used to predict the results while preserving the commonly used functional dependency on the Nusselt number. That is $Nu = CRe^m Pr^n (Pr/Pr_s)^{0.25}$. The least squares method [45] has yielded the following best curve:

$$Nu = 0.0423 Re^{0.99} Pr^{0.21} \left(\frac{Pr}{Pr_s}\right)^{0.25} \quad (12)$$

As shown in Fig. 11c (for R-123) and Fig. 11d (for water) Eq. (12) predicts the experimental results quite well. The MAEs are 9.0% and 16.1% for R-123 and water data, respectively. For water only the results for $G = 505$ kg/m^2 s are mostly outside of the ±20% bar.

5.2. Pressure drop

Single-phase pressure drop over intermediate size micro pin fins ($1 < H/d < 2.5$) at low Reynolds number has been recently discussed by Koşar et al. [24] and Peles et al. [5]. It was concluded that for H/d larger than ~2 (depending on the Reynolds number) endwalls effects do not predominate the friction factor correlation, and long tube correlations can be used with reasonable adequacy. As a validation, the friction factor as a function of the Reynolds number was compared to Gunther and Shaw [46] correlation. The long fin correlation provides good prediction to the experimental data, with an MAE of 14.6% proving the endwalls effects to be insignificant for $H/d = 2.43$ at high laminar Reynolds numbers ($Re > 100$).

The dependency of the pressure drop on the effective heat flux can be used to predict boiling inception and CHF condition [28,47]. It is well documented and explicated that the pressure drop attains a minimum at the onset of significant void (OSV) conditions [39,40,48,49], defined as the conditions, beyond which the bubbles that detach from the heated channel wall can survive condensation

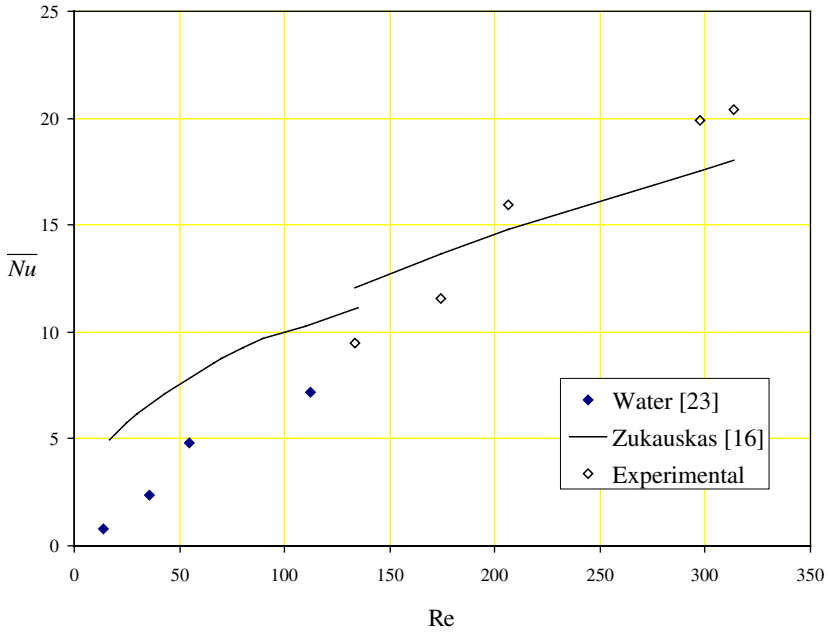

Fig. 10. Average Nusselt number as a function of Reynolds number.

Table 2
Single-phase heat transfer coefficient correlation used in the present study

Correlation number	Reference	Shape and geometry of pin fins, working fluid	Working fluid	Correlation	MAE (%)
1	Zukauskas [16]	Circular, $0.5 < Pr < 500$; $10 < Re < 100$	All fluids	$\overline{Nu} = 0.9Re^{0.4}Pr^{0.36}\left(\frac{Pr}{Pr_s}\right)^{0.25}$	15.5
	Zukauskas [16]	Circular, $0.5 < Pr < 500$; $100 < Re < 1000$	All fluids	$\overline{Nu} = 0.683Re^{0.466}Pr^{0.36}\left(\frac{Pr}{Pr_s}\right)^{0.25}$	

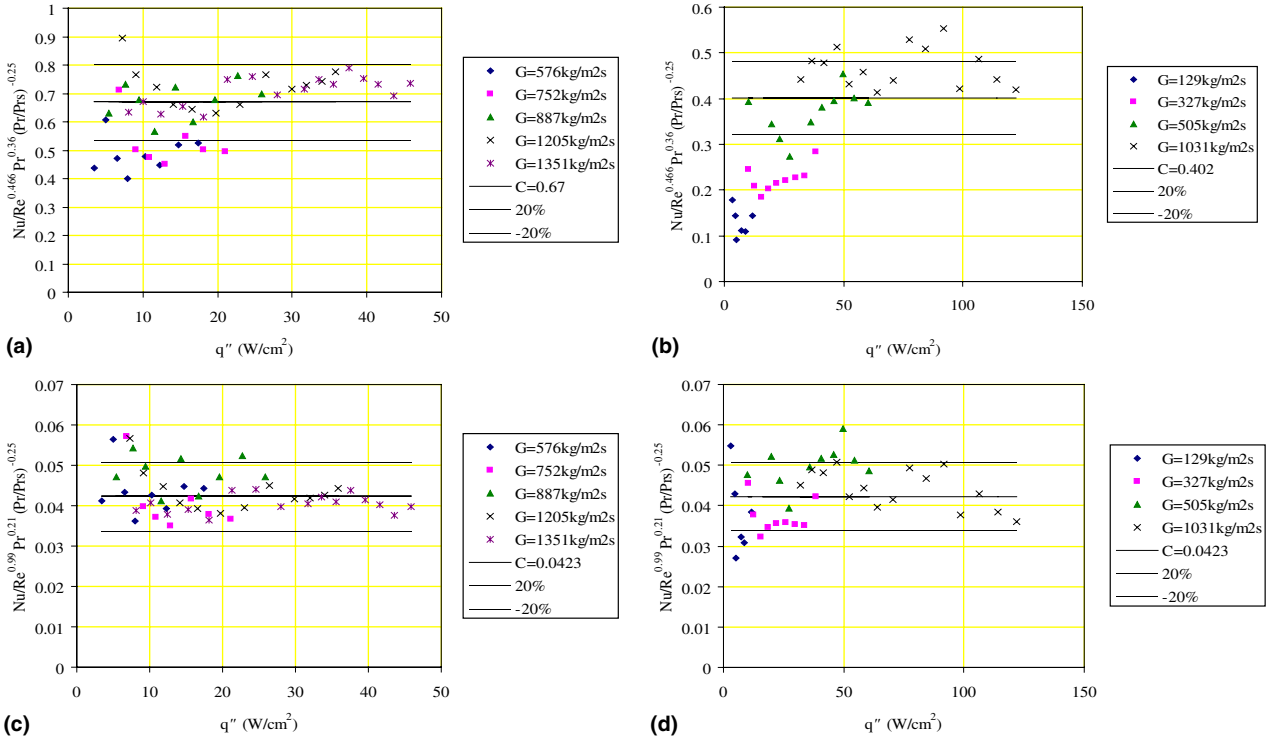

Fig. 11. Predictions of the experimental data (R-123) (a) and the water data [23] (b) by Zukauskas [16] type correlation. Predictions of the experimental data (R-123) (c) and the water data [23] (d) by Eq. (12).

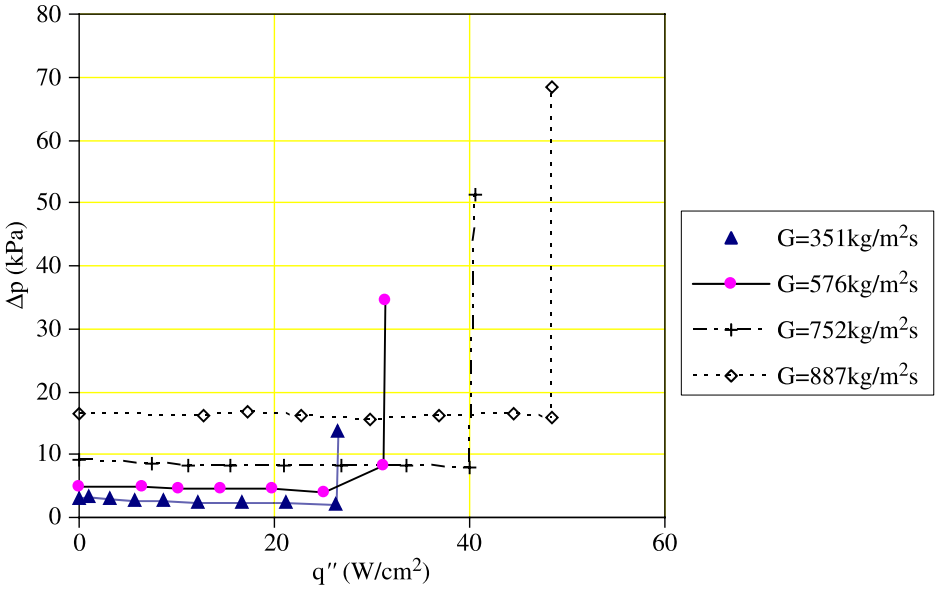

Fig. 12. Pressure drop as a function of heat flux.

sufficiently to cause bulk voidage. An increase in heat flux beyond the OSV conditions results in an increase in the pressure-drop required to maintain a fixed flow rate. With the increase in liquid temperature during single-phase flows, the liquid viscosity drops, which in turn reduces the required pressure drop to maintain constant flow rate, while during two-phase flows the increase in the void fraction increases the pressure drop demand. Fig. 12 shows a similar pattern. The pressure drop demand for a fixed mass flux moderately declines with heat flux. This trend continues until the characteristic minimum is reached, when an abrupt surge in the void fraction is instigated, which in turn rapidly increases the demand for pressure drop. This significant rise in the pressure drop is of great concern in the design of micro heat sinks, since it marks the transition from an efficient hydraulic performance to a very inefficient one. In addition, the emergence of flow instabilities also marks a transition to an ineffective heat transfer mechanism. Thus, heat sink operation under such flow instabilities should be avoided.

6. Conclusions

Single-phase heat transfer, boiling inception, and single- and two-phase pressure drop over a bank of micro pin fins have been studied experimentally and the concomitant results have been discussed in detail. The main conclusions drawn from this investigation are as follows:

- Boiling two-phase flow is excessively suppressed to high liquid temperatures. The increase in onset of nucleate boiling to high temperatures is closely connected to the hydrophilicity of the working fluid on silicon surfaces. R-123 has a near-zero contact angle on silicon, and as a result large nucleation cavities are flooded, which in turn gives rise to high liquid superheat at boiling inception.
- The delay in boiling to high superheats triggers a chain of periodic events. Once boiling is initiated, vapor burst instabilities resembling *compound relaxation instabilities* (specifically *chugging*) are remarkable. To further divulge the extent of this issue, comprehensive experimental studies over assorted surface topographies and chemistries over a range of thermal and hydraulic conditions are imperative.
- With the increase in Reynolds number, particularly for $Re > 100$, endwalls effects diminish, thus existing correlations for long tubes provide a good prediction for the experimental data. At low Reynolds numbers ($Re < 100$), conventional scale correlations considerably underpredict the experimental data.
- A new correlation has been developed to predict the experimental data of water and R-123. It predicts the experimental results with MAEs of 9.0% and 16.1% for R-123 and water data, respectively.
- The pressure drops monotonically decline with heat flux during single-phase flow, and abruptly surge once boiling incepts, as a result of rapid increase of the void fraction.

Acknowledgements

This work was supported by the Office of Naval Research through the Young Investigator Program, under contract No. N00014-05-1-0582 (Program Officer: Dr. Mark Spector). Graduate student support from Rensselaer Polytechnic Institute is also gratefully appreciated. The microfabrication was performed in part at the Cornell NanoScale Facility (a member of the National Nanotechnology Infrastructure Network) which is supported by the National Science Foundation under Grant

ECS-0335765, its users, Cornell University and industrial affiliates. The authors are thankful to Mr. Chandan Mishra and Mr. Brandon Schneider for their valuable suggestions during the development of the CAD model.

References

[1] D.L. Hitt, C.M. Zakrzwski, M.A. Thomas, MEMS-based satellite micropropulsion via catalyzed hydrogen peroxide decomposition, Smart Mater. Struct. 10 (2001) 1163–1175.
[2] A.P. London, A.A. Ayon, A.E. Epstein, S.M. Spearing, T. Harrison, Y. Peles, J.L. Kerrebrock, Microfabrication of a high pressure bipropellant rocket engine, Sensors Actuat. A: Physical 92 (1–3) (2001) 351–357.
[3] C.M. Spadaccini, X. Zhang, C.P. Cadou, N. Miki, I.A. Waitz, Preliminary development of a hydrocarbon-fueled catalytic microcombustor, Sensors Actuat. A: Physical 103 (1–2) (2003) 219–224.
[4] D.H. Lee, S. Kwon, Heat transfer and quenching analysis of combustion in a micro combustion vessel, J. Micromech. Microeng. 12 (5) (2002) 670–676.
[5] Y. Peles, A. Koşar, C. Mishra, C.J. Kuo, B. Schneider, Forced convective heat transfer across a pin fin micro heat sink, Int. J. Heat Mass Transfer 48 (17) (2005) 3615–3627.
[6] D.B. Tuckerman, R.F.W. Pease, High-performance heat sinking for VLSI, IEEE Electron Dev. Lett. EDL-2 (5) (1981) 126–129.
[7] R.W. Knight, D.J. Hall, J.S. Goodling, R.C. Jaeger, Heat sink optimization with application to microchannel, IEEE Trans. Comp., Hybrids Manufact. Technol. (15) (1992) 832–842.
[8] S. Lee, Optimum design and selection of heat sinks, IEEE Trans. Comp. Packag., Manufact. Technol. A (18) (1995) 812–817.
[9] M.B. Kleiner, S.A. Kühn, K. Harberger, High performance forced air cooling scheme employing microchannel heat exchangers, IEEE Trans. Comp. Packag., Manufact. Technol. A (18) (1995) 795–804.
[10] C. Gilliot, C. Schaeffer, A. Bricard, Integrated micro heat sink for power multichip module, IEEE Trans. Ind. Appl. 36 (1) (2000) 217–221.
[11] L.R. Arana, S.B. Schaevitz, A.J. Franz, M.A. Schmidt, K.F. Jensen, Microfabricated suspended-tube chemical reactor for thermally efficient fuel processing, J. Microelectromech. Syst. 12 (5) (2003) 600–612.
[12] M.W. Losey, J. Jackman, S.L. Firebaugh, M.A. Schmidt, K.F. Jensen, Design and fabrication of microfluidic devices for multiphase mixing and reaction, J. Microelectromech. Syst. 11 (6) (2002) 709–717.
[13] A.H. Epstein, S.D. Senturia, Macro power from micro machinery, Science 276 (5316) (1997) 1211.
[14] A.P. London, Ph.D. thesis, Development and test of a microfabricated bipropellant rocket engine, Cambridge, MA, USA, 2000.
[15] E.M. Sparrow, J.P. Abraham, J.C.K. Tong, Archival correlations for average heat transfer coefficients for non-circular and circular cylinders and for spheres in cross-flow, Int. J. Heat Mass Transfer 47 (24) (2004) 5285–5296.
[16] A.A. Zukauskas, Heat transfer from tubes in cross flowAdvances in Heat Transfer, 8, Academic Press, New York, 1972, pp. 93–160.
[17] S. Whitaker, Forced convection heat-transfer correlations for flow in pipes, past flat plates, single cylinders, single spheres, and for flow in packed-beds and tube bundles, AIChE J. 18 (2) (1972) 361–371.
[18] T. Igarashi, Fluid flow and heat transfer around rectangular cylinders (the case of a width/height ratio of a section of 0.33–1.5), Int. J. Heat Mass Transfer 30 (1987) 893–901.
[19] M.K. Chyu, Y.C. Hsing, V. Natarajan, Convective heat transfer of cubic fin arrays in a narrow channel, J. Heat Transfer 120 (1998) 362–367.
[20] E.M. Sparrow, V.B. Grannis, Pressure drop characteristics of heat exchangers consisting of arrays of diamond-shaped pin fins, Int. J. Heat Mass Transfer 34 (3) (1991) 589–600.
[21] O.N. Şara, Performance analysis of rectangular ducts with staggered square pin fins, Energy Conserv. Manage. 144 (2003) 1787–1803.
[22] C. Marques, K.W. Kelly, Fabrication and performance of a pin fin micro heat exchanger, J. Heat Transfer 126 (3) (2004) 434–444.
[23] A. Koşar, Y. Peles, Thermal-hydraulic performance of MEMS-based pin fin heat sink, J. Heat Transfer 128 (2) (2006) 121–131.
[24] A. Koşar, C. Mishra, Y. Peles, Laminar flow across a bank of low aspect ratio micro pin fins, J. Fluids Eng. 127 (3) (2005) 419–430.
[25] B. Schneider, M.S. thesis, Hydrodynamic characteristics of cross flow over MEMS-based pillars, Rensselaer Polytechnic Institute, Troy, NY, USA, 2005.
[26] A. Koşar, Ph.D. thesis, Heat and Fluid Flow in micro pin fin heat sinks, Rensselaer Polytechnic Institute, Troy, NY, USA, 2006.
[27] S. Kline, F.A. McClintock, Describing uncertainties in single-sample experiments, Mech. Eng. 75 (1) (1953) 3–8.
[28] S. Van Stralen, R. Cole, Boiling Phenomena, Hemisphere Publication Corporation, New York, 1979, pp. 71–88.
[29] A.E. Bergles, Elements of Boiling Heat Transfer-Modern Development and Advances, Elsevier Science Publishers, Amsterdam, 1992, pp. 389–445.
[30] A.E. Bergles, S.G. Kandlikar, On the nature of critical heat flux in microchannels, J. Heat Transfer 127 (2005) 101–107.
[31] A. Koşar, C.J. Kuo, Y. Peles, Reduced pressure boiling heat transfer in rectangular microchannels with interconnected reentrant cavities, J. Heat Transfer 127 (10) (2005) 1106–1114.
[32] A. Koşar, C.J. Kuo, Y. Peles, Boiling heat transfer in rectangular microchannels with reentrant cavities, Int. J. Heat Mass Transfer 48 (23) (2005) 4867–4886.
[33] L. Zhang, E.N. Wang, K.E. Goodson, T.W. Kenny, Phase change phenomena in silicon microchannels, Int. J. Heat Mass Transfer 48 (8) (2005) 1572–1582.
[34] J.A. Bouré, A.E. Bergles, L.S. Tong, Review of two-phase flow instability, Nucl. Eng. Des. 25 (1973) 165–192.
[35] J.G. Collier, J.R. Thome, Convective Boiling and Condensation, third ed., Oxford Science Publications, Oxford, 1994.
[36] E.J. Davis, G.H. Anderson, The incipience of nucleate boiling in forced convection flow, AIChE J. 12 (4) (1966) 774–780.
[37] Y.Y. Hsu, R.W. Graham, Transport Processes in Boiling and Two-phase Systems, Hemisphere Publication Corporation, Washington DC, 1976.
[38] K. Cornwell, P.A. Kew, Boiling in small parallel channels, Energy Efficiency Process Technol. 37 (2) (1992) 624–638.
[39] J.E. Kennedy, G.M. Roach Jr, M.F. Dowling, S.I. Abdel-Khalik, S.M. Ghiaasiaan, S.M. Jeter, Z.H. Quershi, The onset of flow instability in uniformly heated horizontal microchannels, J. Heat Transfer 122 (1) (2000) 118–125.
[40] S.G. Kandlikar, M.E. Steinke, S. Tian, L.A. Campbell, High-speed photographic observation of flow boiling of water in parallel microchannels, Paper presented at the ASME National Heat Transfer Conference, ASME, June 2001.
[41] W. Qu, I. Mudawar, Measurement and prediction of pressure drop in two-phase microchannel heat sinks, Int. J. Heat Mass Transfer 46 (15) (2003) 2737–2753.
[42] A.E. Bergles, S.G. Kandlikar, Critical heat flux in microchannels: experimental issues and guidelines for measurement, in: First International Conference on Microchannels and Minichannels, Rochester, New York, April 24–25, 2003, pp. 141–147.
[43] D.D. Brutin, F. Topin, L. Tadrist, On thermo-hydraulic instabilities in small channels during flow boiling, in: Experimental Heat Transfer, Fluid Mechanics, and Thermodynamics, ETS, Pisa, Italy, 2001, pp. 273–289.
[44] S.S. Mehendale, A.M. Jacobi, R.K. Shah, Fluid flow and heat transfer at micro- and meso-scales with application to heat exchanger design, Appl. Mech. Rev. 53 (7) (2000) 175–193.
[45] J.H. Mathews, Numerical Methods for Mathematics, Science, and Engineering, Prentice Hall, 1992, pp. 257–314.
[46] A.Y. Gunter, W.A. Shaw, A general correlation of friction factors for various types of surfaces in cross flow, Trans. Amer. Soc. Mech. Engrs. 67 (1945) 643–660.

[47] R.A. Pabisz, A.E. Bergles, Using pressure drop to predict the critical heat flux in multiple tube, subcooled boiling systems, Exper. Boiling Heat Transfer 2 (1997) 851–858.
[48] G.M. Roach, S.I. Abdel-Khalik, S.M. Ghiaasiaan, M.F. Dowling, S.M. Jeter, Low-flow-onset of flow instability in heated microchannels, Nucl. Sci. Eng. 133 (1) (1999) 106–117.
[49] R.M. Stoddard, A.M. Blasick, S.M. Ghiaasiaan, S.I. Abdel-Khalik, S.M. Jeter, M.F. Dowling, Onset of flow instability and critical heat flux in thin horizontal annuli, Exper. Thermal Fluid Sci. 26 (1) (2002) 1–14.